Tunable permalloy-based films for magnonic devices

Yuli Yin,[1,2,3,*] Fan Pan,[3,4] Martina Ahlberg,[2] Mojtaba Ranjbar,[2] Philipp Dürrenfeld,[2] Afshin Houshang,[2] Mohammad Haidar,[2] Lars Bergqvist,[3,4] Ya Zhai,[1] Randy K. Dumas,[2] Anna Delin,[3,4,5] and Johan Åkerman[2,3]

[1]*Department of Physics, Southeast University, 211 189 Nanjing, China*

[2]*Department of Physics, University of Gothenburg, SE-41296 Gothenburg, Sweden*

[3]*Department of Materials and Nano Physics, School of Information and Communication Technology, KTH Royal Institute of Technology, Electrum 229, SE-16440 Kista, Sweden*

[4]*SeRC (Swedish e-Science Research Center), KTH Royal Institute of Technology, SE-10044 Stockholm, Sweden*

[5]*Department of Physics and Astronomy, Materials Theory Division, Uppsala University, Box 516, SE-75120 Uppsala, Sweden*

(Received 25 March 2015; revised manuscript received 5 June 2015; published 27 July 2015)

Using both broadband ferromagnetic resonance (FMR) spectroscopy and *ab initio* calculations, we study the magnetodynamic properties of permalloy (Py, $Ni_{80}Fe_{20}$) and $Py_{100-x}M_x$ films with M as platinum (Pt), gold (Au), or silver (Ag). From the uniform FMR mode, we extract the saturation magnetization (M_S), damping (α), and inhomogeneous broadening (ΔH_0); from the first perpendicular standing spin-wave (PSSW) mode, we extract the exchange stiffness (A). M_S and A are found to decrease with increasing alloying, most strongly for Au and less so for Pt. On the other hand, α increases rapidly with both Pt and Au content, while being virtually independent of Ag content. The physical origins of the observed trends in α, M_S, and A are analyzed and explained using density functional theory calculations in the coherent potential approximation. The calculated trends quantitatively agree with the experimental observations. The drastically different impacts of Pt, Au, and Ag on the various fundamental magnetodynamic properties will allow for significant design freedom, where different properties can be varied independently of others through careful combinations of the Pt, Au, and Ag contents of $Py_{100-x}M_x$ films. By empirical approximations of each property's concentration dependence, we can dial in any desired combination of magnetodynamic properties within this parameter space. As a proof-of-principle demonstration we design a set of $Py_{100-x-y}Pt_xAg_y$ films, where the saturation magnetization stays constant throughout the set and the damping can be tuned by a factor of 4.

DOI: 10.1103/PhysRevB.92.024427 PACS number(s): 75.70.−i, 76.50.+g, 71.15.Mb

I. INTRODUCTION

The magnetodynamic properties of magnetic thin films are central to the emerging research field of magnonics [1,2]. Since Bloch's original description of spin waves [3] (SWs), and the subsequent first direct measurement of the uniform ferromagnetic resonance [4] (FMR), the primary focus has been on long wavelength and low amplitude SWs. In this so-called magnetostatic approximation [5,6], the SW dispersion is governed by dipolar interactions, and the most important material parameters for describing SW dynamics are the saturation magnetization (M_S), any existing anisotropy field, and the spin-wave damping (α). For thin-film applications, the dominant magnetic metal has been permalloy (Py), due to its low coercivity, low magnetocrystalline anisotropy, low magnetostriction, and low α. A number of recent studies have reported that M_S and α in Py can be tailored using alloying with transition and rare-earth metals: Rantschler *et al.* [7] studied the effect of doping on the magnetic damping of Py, and found stronger effects for heavier elements, which suggests that spin-orbit coupling is an important aspect. Woltersdorf *et al.* [8] conducted a study on Py doped with rare-earth metals and explained that the increased damping stemmed from slow-relaxing impurities.

When the wavelength of the SWs is reduced, their energy is increased and their dispersion is modified by exchange interactions. At moderate wave vectors ($\boldsymbol{k}$), magnetostatic SWs give way to dipole-exchange SWs, and if the wavelength is further reduced, they are replaced by entirely exchange-dominated SWs [9]. In these regimes, the exchange stiffness (A) also needs to be known in order to correctly describe the spin-wave dynamics. With the recent exploration of spin-transfer torque (STT) [10–12], it has become relatively straightforward to create exchange-dominated propagating SWs [13–19] and localized magnetodynamic excitations, such as the spin-valve bullet [17–24] and the magnetic droplet [25–31]. These strongly nonlinear SW modes are the foundation of both nanocontact spin-torque nano-oscillators [32–37] (STNOs) and spin-Hall nano-oscillators [38–42] (SHNOs), with promising applications both as stand-alone microwave signal generators and as spin-wave injectors in magnonic devices [43–45]. To tailor these devices, it is necessary to control not only M_S and α, but also A. In two recent studies, Lepadatu *et al.* reported that alloying with V and Gd can reduce A, as extracted indirectly from domain-wall pinning strengths [46,47]. However, it would be particularly useful to be able to control M_S, α, and A *independently*, for example by alloying with different elements that have different impacts on each of the parameters.

We report on a systematic study of M_S, α, A, and the anisotropic magnetoresistance (AMR) of Py films alloyed with the three heavy metals Pt, Au, and Ag. Using broadband FMR spectroscopy, we determine M_S and α from the uniform ($\boldsymbol{k} = 0$) FMR mode and A from the first perpendicular standing spin-wave [48–50] (PSSW) resonance. We find that M_S and A decrease with increasing alloying, more significantly for Au and Ag, and least for Pt. Whereas α increases rapidly with

*Corresponding author: yuri@seu.edu.cn

increasing Pt content, the dependence on Au content is more moderate, and is virtually independent of Ag content. As a consequence, co-alloying with Pt, Au, and Ag in different proportions defines a three-dimensional parameter space where M_S, α, and A can be varied independently, within certain limits. To demonstrate this possibility, we design a set of $Py_{100-x-y}Pt_xAg_y$ films targeting a constant M_S and a damping varying by a factor of 4, which we then confirm experimentally.

Ab initio calculations using the coherent potential approximation (CPA) reproduce these overall results and provide deeper insight into the experimental trends. In particular, the physical origins of the trends in the observed parameters are qualitatively explained by analyzing the differences in magnetic susceptibility, exchange, chemical bonding, and the spin-orbit coupling of Pt, Au, and Ag.

II. EXPERIMENTAL METHODOLOGY

Magnetic films (100 nm thick) of $Py_{100-x}M_x$, with M either Pt, Au, or Ag, $x = 10$–$30\,\%$, and the nominal composition of Py being $Ni_{80}Fe_{20}$, were co-sputtered on glass and Si/SiO_2 substrates. Room temperature magnetron sputtering deposition was performed in a high-vacuum chamber with a base pressure of less than 3×10^{-8} Torr. The argon working pressure was 3 mTorr with a 30 sccm gas flow during deposition; alloy compositions were established by varying the plasma power of the heavy metal targets between 10 and 85 W, while keeping the Py sputtering power at 400 W. A pure Py film served as a reference. For protection, all films were capped *in situ* with a 10-nm-thick SiO_2 layer by rf magnetron sputtering. Energy dispersive x-ray spectroscopy (EDX) confirmed that the nominal atomic compositions were within ± 3 atomic percent. Broadband ferromagnetic resonance (FMR) measurements were carried out using a NanOsc Instruments PhaseFMR with a 200-μm-wide coplanar waveguide (CPW). The samples were placed face down on the CPW (inset of Fig. 1) and subjected to a microwave field h with frequencies between 3 and 16 GHz. An in-plane magnetic field H was applied perpendicular to h and swept from 0 to 3.5 kOe. AMR measurements were performed using a four-point probe technique in a rotating 1 kOe in-plane magnetic field. All measurements were carried out at room temperature.

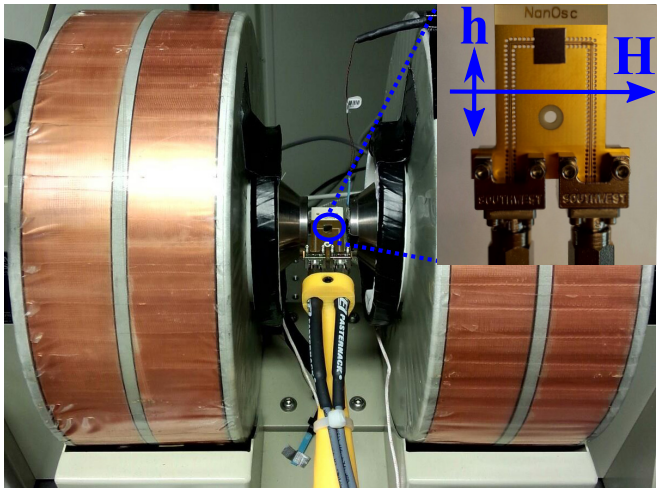

FIG. 1. (Color online) The FMR measurement setup consisting of the coplanar waveguide inside the electromagnet. Inset: Top view of coplanar waveguide, showing the directions of the static (H) and microwave (h) fields.

III. COMPUTATIONAL METHODOLOGY

Spin-polarized electronic structure calculations within density functional theory (DFT) of the ground state of doped Py were performed using the multiple-scattering Korringa-Kohn-Rostoker (KKR) Green's function framework [51,52] and the coherent potential approximation (CPA). The generalized gradient approximation (GGA) was employed for the exchange correlation potential, and relativistic effects were fully taken into account by solving the Dirac equation for both the core and valence electrons. By calculating the total energy as a function of volume, the equilibrium lattice constant can be identified with the minimum total energy for a given impurity concentration. Magnetic exchange interactions J_{ij} within a Heisenberg model were calculated using the magnetic force theorem [53,54] for all interatomic distances up to 5 lattice constants. The exchange spin-wave stiffness $D = \frac{2\mu_B}{3m}\sum_j J_{0j}R_{0j}^2$, where m is the magnetic moment per atom and R_{0j} is a vector connecting the sites 0 and j, was determined from the calculated Heisenberg exchange coupling parameters J_{ij}. We applied the methodology suggested by Pajda *et al.* [55] to avoid a numerically nonconvergent sum: The spin-wave stiffness oscillates as a function of the number of coordination shells. By introducing a damping parameter η and taking the limit as $\eta \to 0$, the sum can be made to converge. The exchange spin-wave stiffness D is converted to the micromagnetic exchange stiffness A through the relation $A = Dm_S(T)/(2g\mu_B)$, where m_S is the calculated saturation magnetic moment at temperature T, g is the gyromagnetic ratio of the electron, and μ_B is the Bohr magneton [56]. The Gilbert damping parameter was calculated within the linear response formalism [57–59], where the vertex corrections were included using a dense mesh of 1.2×10^7 k points distributed over the full Brillouin zone. In addition, to be consistent with room-temperature experimental conditions, it was necessary to take into account the temperature effects of the magnetization and of the Gilbert damping parameter. Room temperature magnetization was obtained by mapping the exchange coupling constants and magnetic moments at zero temperature to the Heisenberg Hamiltonian and applying Monte Carlo simulations using the Metropolis algorithm [60] in the UPPASD program [61]. The temperature dependence of the Gilbert damping parameter was also taken into account by including additional scattering due to phonons at finite temperatures, as described in [58] and [59]. The additional contribution from magnons was also calculated with a very similar method as the one used for the phonon contribution [62].

IV. RESULTS AND DISCUSSION

A. FMR and PSSW measurements

Whereas the fundamental FMR mode is characterized by a magnetization precession that is uniform both laterally and through the film thickness, the PSSW mode is laterally uniform but forms a standing spin wave through the film

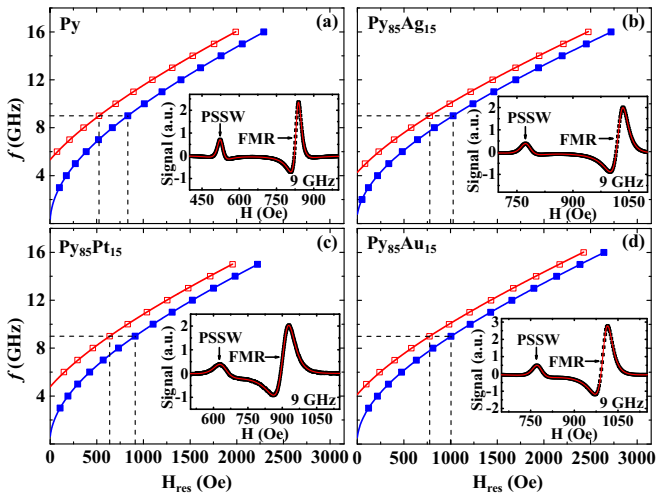

FIG. 2. (Color online) Frequency of the uniform mode (blue points) and the first PSSW mode (red points) as a function of field for (a) Py, (b) $Py_{85}Ag_{15}$, (c) $Py_{85}Pt_{15}$, and (d) $Py_{85}Au_{15}$. Solid lines are fits to Eq. (2). Dashed lines mark the resonance field of the FMR mode and the first PSSW modes at 9 GHz as extracted from the full field scans, which are shown in the insets. Red solid lines in the insets are fits to Eq. (1).

thickness. Typical measurements of both resonances are shown in the insets in Fig. 2 with the PSSW mode appearing at lower fields due to the additional exchange energy of its nonuniform precession. The full spectrum can be accurately fit with a sum of symmetrical and antisymmetrical Lorentzian derivates [63,64],

$$S = \frac{d}{dH}\left\{\frac{K_1\Delta H_F{}^2 + K_2\Delta H_F(H-H_F)}{\Delta H_F^2 + 4(H-H_F)^2}\right\} + \frac{d}{dH}\left\{\frac{K_3\Delta H_P{}^2 + K_4\Delta H_P(H-H_P)}{\Delta H_P^2 + 4(H-H_P)^2}\right\}, \quad (1)$$

where H_F, ΔH_F, H_P, and ΔH_P are the resonance fields and linewidths of the FMR and PSSW mode respectively. K_1 and K_3 are the coefficients of the symmetrical Lorentzian functions, and K_2 and K_4 are the respective parameters of the antisymmetrical Lorentzian functions.

The field dependence of the extracted FMR and PSSW resonance frequencies are shown in Fig. 2 for Py, $Py_{85}Ag_{15}$, $Py_{85}Pt_{15}$, and $Py_{85}Au_{15}$, together with fits to the equation [65,66],

$$f = \frac{\gamma\mu_0}{2\pi}\left[\left(H_{\rm res} + H_k + \frac{2A}{\mu_0 M_S}\left(\frac{p\pi}{d}\right)^2\right) \times \left(H_{\rm res} + \frac{2A}{\mu_0 M_S}\left(\frac{p\pi}{d}\right)^2 + M_S + H_k\right)\right]^{1/2}, \quad (2)$$

where $H_{\rm res}$ is the magnetic resonance field of either the FMR ($p = 0$) or the PSSW mode ($p = 1$), γ is the gyromagnetic ratio, H_k is the in-plane anisotropy field, μ_0 is the permeability of free space, and d is the thickness of the film. From such fits, we first extracted M_S, γ, and H_k from the FMR mode, and then used these values when extracting A from the PSSW mode. The mode number used in Eq. (2) is based on boundary conditions where

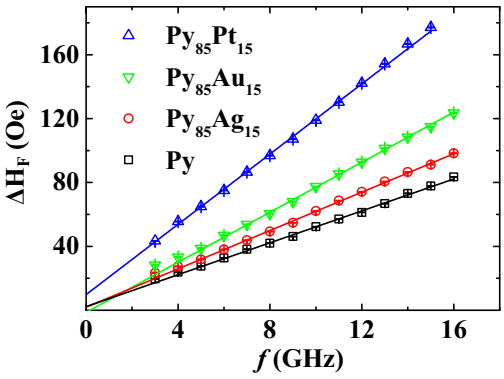

FIG. 3. (Color online) FMR linewidth ΔH_F for $Py_{85}Pt_{15}$, $Py_{85}Au_{15}$, $Py_{85}Ag_{15}$, and Py films. The solid lines are fits to Eq. (3). Note that the error bars are smaller than the data points.

there is no pinning at the interfaces. This assumption can be rationalized by the in-plane geometry of the measurement and the nonuniformity of the excitation field across the film thickness [67–71]. The frequency-dependent FMR linewidths of the same films (Fig. 3) can be well fit using [7,8]

$$\Delta H_F = \Delta H_0 + \frac{4\pi\alpha}{\gamma} f, \quad (3)$$

where ΔH_0 is the inhomogeneous broadening, and α is the Gilbert damping coefficient. Two-magnon scattering (TMS) can give substantial contributions to the measured linewidth, leading to overestimated values of the damping [72]. However, we do not observe any changes in $\Delta H(f)$ consistent with TMS, not even in frequencies up to 40 GHz (not shown). We therefore conclude that the TMS is negligible in our films.

The in-plane anisotropy is as expected very small in all samples, typically a few oersteds. The determined values of $M_S = 0.9$ T and $A = 1.1 \times 10^{-11}$ J/m of our reference Py films are consistent with literature values [19,73–75]. Similarly, the values of α and M_S of our 100-nm-thick $Py_{90}Pt_{10}$ film are close to the values reported by Ingvarsson *et al.* [76] for 50-nm-thick films. The relevant parameters extracted from the fits are listed in Table I.

B. M_S, A, and α vs film composition

The intrinsic Gilbert damping of the FMR mode as a function of film composition is plotted in Fig. 4(a) alongside DFT calculations in Fig. 4(d). While the damping trend of the $Py_{100-x}Ag_x$ or $Py_{100-x}Au_x$ films has a linear dependence on concentration, the $Py_{100-x}Pt_x$ samples show a more quadratic behavior. On one hand, alloying with Pt has the strongest effect on damping, leading to a maximum value of $\alpha = 0.035$ at 30 at. %, i.e., about 4.5 times the value of the pure Py film. On the other hand, the damping in $Py_{100-x}Ag_x$ films is virtually independent of composition. The trends are in good agreement with what Rantschler *et al.* showed in [7], where they pointed out that heavier element impurities more strongly affect damping, indicating that spin-orbit coupling is a major source of the increase in damping. The calculated Gilbert damping parameters, Fig. 4(d), agree well with previously available calculations in the literature. For pure Py, we obtain $\alpha = 0.0036$ with only the phonon contribution

TABLE I. Extracted parameters of the magnetodynamic properties of alloyed $Py_{100-x}M_x$, where M is Pt, Ag, or Au. The additional uncertainty in the thickness of the films (±3 nm) is taken into account in the uncertainty of A.

$Py_{100-x}M_x$	x (at.%)	$\mu_0 M_S$ (T)	$\gamma/2\pi$ (GHz/T)	α (10^{-3})	ΔH_0 (Oe)	A (10^{-12} J/m)
Py	0	0.905 ± 0.012	31.4 ± 0.2	7.8 ± 0.2	2.3 ± 0.9	11.30 ± 0.15
M=Pt	10	0.853 ± 0.011	31.0 ± 0.2	14.4 ± 0.2	6.0 ± 0.7	9.21 ± 0.58
	15	0.843 ± 0.014	30.8 ± 0.3	16.9 ± 0.2	9.8 ± 0.8	9.22 ± 0.63
	20	0.787 ± 0.016	31.0 ± 0.3	22.6 ± 0.3	13.8 ± 1.1	8.05 ± 0.53
	25	0.771 ± 0.023	30.6 ± 0.4	29.0 ± 0.4	16.9 ± 1.6	7.07 ± 0.50
	30	0.722 ± 0.019	30.7 ± 0.3	35.3 ± 0.4	20.2 ± 1.0	6.87 ± 0.52
M=Au	10	0.766 ± 0.005	31.6 ± 0.1	11.3 ± 0.2	− 1.2 ± 1.1	6.93 ± 0.49
	15	0.706 ± 0.006	31.5 ± 0.1	12.4 ± 0.2	− 1.3 ± 1.1	6.62 ± 0.45
	20	0.608 ± 0.005	31.5 ± 0.1	13.2 ± 0.2	3.4 ± 1.0	5.12 ± 0.36
	25	0.537 ± 0.003	31.5 ± 0.1	15.3 ± 0.1	0.3 ± 0.5	4.16 ± 0.30
	30	0.460 ± 0.003	31.5 ± 0.1	17.1 ± 0.1	2.1 ± 0.5	3.03 ± 0.23
M=Ag	15	0.758 ± 0.006	30.2 ± 0.1	9.1 ± 0.2	2.1 ± 0.8	7.57 ± 0.51
	20	0.654 ± 0.005	30.1 ± 0.1	9.5 ± 0.2	4.2 ± 0.9	5.84 ± 0.37
	25	0.617 ± 0.006	30.1 ± 0.2	9.5 ± 0.2	12.0 ± 1.1	4.18 ± 0.32
	30	0.517 ± 0.007	30.6 ± 0.2	10.3 ± 0.3	15.8 ± 1.7	3.11 ± 0.22

included at finite temperature, increasing to $\alpha = 0.0040$ when an additional magnon contribution is included, compared to $\alpha = 0.0046$ obtained in [77]. For a 10 at. % concentration of Pt and Au, our calculated values are close to those found in [58] and [59] using the same methodology. Including the additional magnon contribution to the Gilbert damping on top of the phonon contribution results in a decrease (<10%) in the calculated values for Ag and Au, while it plays a more important role for Pt, where the Gilbert damping increases by up to 30%. Although the spin-orbit coupling is a major factor in determining the Gilbert damping, it cannot be the only factor, since that would imply that Pt and Au have similar trends in the Gilbert damping parameter as a function of impurity concentration. Instead, it is clear from Fig. 4(d) that the increase in Gilbert damping is much more pronounced for Pt than for Au. This can be explained by examining the differences in the electronic structure of Au and Pt. The 5d band in Au is filled, and Au therefore has virtually only sp states at the Fermi level. For Pt, on the other hand, there is a substantial contribution to the density of states (DOS) at the Fermi level from the partially unfilled 5d band. The larger DOS at the Fermi level for Pt leads to increased scattering, and thus larger Gilbert damping [59]. Ag has a filled 4d band and so, compared with Au, a very similar electronic structure at the Fermi level, consisting of predominantly sp states. Furthermore, the spin-orbit coupling in 4d systems (like Ag) is much smaller than in 5d systems (such as Au). Together, this explains the trend observed in the Gilbert damping as a function of Ag concentration. For Ag, the lack of both substantial spin-orbit coupling and d states at the Fermi level result in a Gilbert damping virtually independent of Ag concentration. The damping parameter per atomic percentage $\Delta\alpha_M$ can be empirically characterized, according to the relation [7,8] $\alpha = \alpha_0 + \Delta\alpha_M x$, where $\alpha_0 = 0.008$ is the damping of undoped Py, and x is the doping concentration in atomic percent. However, the damping of the $Py_{100-x}Pt_x$ series does not follow a linear trend and is therefore fit to the quadratic relation $\alpha = \alpha_0 + \Delta\alpha_M x + Cx^2$. All the parameters extracted from the empirical fittings are shown in Table II.

Figures 4(b) and 4(e) show the composition dependencies of M_S, where M_S is found to decrease with increasing alloying, the most for Au and the least for Pt. M_S of $Py_{100-x}M_x$ samples show a parabolic decrease and were fit to a quadratic expression, $M = M_0 + \Delta M_M x + Dx^2$, where $\mu_0 M_0 = 0.9$ T

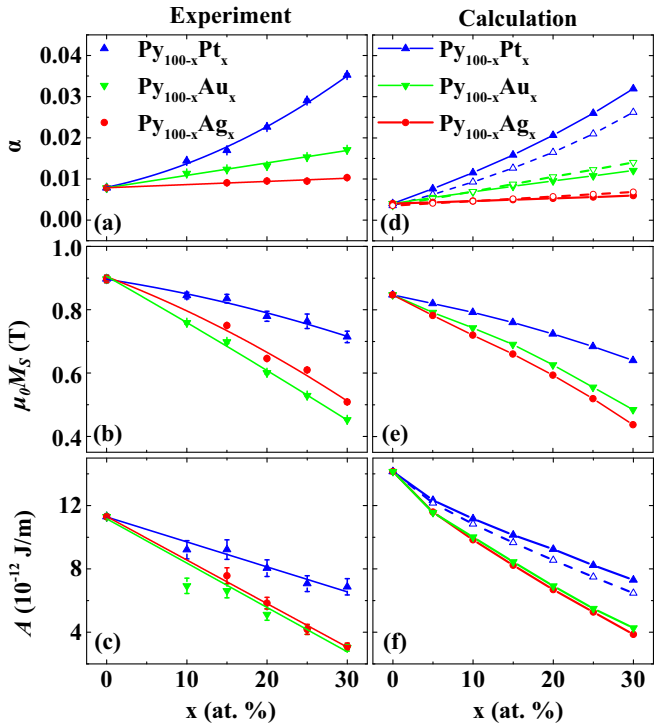

FIG. 4. (Color online) Left: experimental results for (a) damping, (b) saturation magnetization, and (c) exchange stiffness as a function of Pt, Au, and Ag concentration. Solid lines are empirical fits to second-order polynomials. Right: the same parameters calculated using DFT at room temperature. Solid symbols in (d) include both magnon and phonon contributions, while open symbols include phonons only. Solid symbols in (f) include exchange interactions between M and Py, whereas open triangles (Pt) ignore those. Solid and dashed lines in (d), (e), and (f) are visual guides.

TABLE II. Extracted parameters of empirical fittings of alloyed $Py_{100-x}M_x$, where M is Pt, Ag, or Au.

$Py_{100-x}M_x$	$\Delta\alpha_M(10^{-5}\frac{1}{\text{at.\%}})$	$C(10^{-5}\frac{1}{(\text{at.\%})^2})$	$\mu_0\Delta M_M(10^{-3}\frac{\text{T}}{\text{at.\%}})$	$\mu_0 D(10^{-3}\frac{\text{T}}{(\text{at.\%})^2})$	$\Delta A_M(10^{-12}\frac{\text{J}}{\text{m at.\%}})$
M=Pt	41.0	1.6	−3.9	−0.07	−0.16
M=Au	30.2		−14.4	−0.03	−0.28
M=Ag	7.7		−9.6	−0.11	−0.28

is the saturation magnetization of undoped Py. A reduction in M_S is expected, as the proportion of magnetic material decreases with increasing alloying. Furthermore, the observed and calculated trends can be qualitatively understood through a simple argument involving the magnetic susceptibilities of the impurity atoms. Au and Ag are slightly diamagnetic, with the calculated magnetic susceptibilities of $\chi_{\text{m,Au}} = -3.4 \times 10^{-5}$ and $\chi_{\text{m,Ag}} = -2.6 \times 10^{-5}$, respectively, whereas Pt is paramagnetic with an unusually large magnetic susceptibility for a nonmagnetic metal of $\chi_{\text{m,Pt}} = 26 \times 10^{-5}$. According to our CPA calculations, Au and Ag impurities have minute (effectively zero) magnetic moments ($0.018\,\mu_B$ for Au and $-0.011\,\mu_B$ for Ag), whereas the Pt impurities result in an induced magnetic moment of $0.22\,\mu_B$ in the direction of the magnetization.

The composition dependence of the exchange stiffness A is given in Figs. 4(c) and 4(f), where A decreases rapidly in the case of the $Py_{100-x}Ag_x$ and $Py_{100-x}Au_x$ films, but not as much for $Py_{100-x}Pt_x$. Each data set is fit to the equation $A = A_0 + \Delta A_M x$, where $A_0 = 1.1 \times 10^{-11}$ J/m is the exchange stiffness of pure Py. Just as for the damping and saturation magnetization, the calculated exchange stiffness agrees very well with the experimental data.

In order to elucidate why the exchange stiffness decreases less quickly with concentration in Pt, as compared to Ag and Au, we performed an additional calculation of the exchange stiffness in which the M-Py hybridization was kept intact, but all exchange interactions between M and Py were removed. This caused the behavior of the exchange stiffness in the case of Pt to decrease somewhat, as illustrated by the blue unfilled triangles in Fig. 4(f). Therefore, we can conclude that the exchange interaction between the Pt $5d$ states and the Py is one of several factors driving the observed trend. At zero temperature, it is the dominant factor (data not shown).

C. Anisotropic magnetoresistance

For some magnonic devices, such as SHNOs, a high AMR is crucial for the electrical detection of auto-oscillations [39]. It also contributes significantly to the mixing voltage in spin pumping experiments [78]. Therefore, AMR measurements were performed with the magnetization rotated in the film plane with respect to the current direction. The inset of Fig. 5 illustrates the dependence of the magnetoresistance (MR) on the angle φ between the direction of magnetization and the current orientation for the $Py_{85}Pt_{15}$ sample. The red solid line is a fit to the well-known cosine dependence [79,80] $\rho = \rho_\perp + (\rho_\parallel - \rho_\perp)\cos^2\varphi$, where $\rho_\parallel$ and $\rho_\perp$ denote the resistivity when the magnetization direction is parallel ($\varphi = 0^\circ$) and perpendicular ($\varphi = 90^\circ$) to the current orientation, respectively. The AMR is then determined by the relation $\Delta\rho/\rho = (\rho_\parallel - \rho_\perp)/\rho_\perp$. The composition dependencies of AMR are shown in Fig. 5. The effects of dopant M on the AMR ratio are strongly dependent on the concentration x, with AMR ratios decreasing as the concentrations increase. The AMR ratios of $Py_{100-x}Ag_x$ drop most quickly, and most slowly for $Py_{100-x}Au_x$. The AMR of pure Py is measured to be 2.2%, which is in accordance with previously reported values [79,81].

D. Tunable $Py_{100-x-y}Pt_xAg_y$ films with desired magnetodynamic properties

As discussed above for the $Py_{100-x}M_x$ films, M_S and A are found to decrease with increasing alloying, more strongly for Ag and less so for Pt. On the other hand, α increases rapidly with Pt content, while being virtually independent of Ag content. Consequently, we will now show how it is possible to independently tune the parameters M_S, α, and A by dialing in the desired concentrations of Pt and Ag in the ternary alloy system $Py_{100-x-y}Pt_xAg_y$. The results from the empirical quadratic fits to the saturation magnetization, as given in Table II, allow us to calculate Pt and Ag concentrations (x_{Pt} and y_{Ag}) for which M_S is expected to have a constant value. The results of these calculations are shown in Fig. 6(a) as a contour plot for a selected number of different $\mu_0 M_S$. To experimentally verify this model, we deposited a set of five 100-nm-thick films by co-sputtering onto Si/SiO_2 substrates: $Py_{84}Ag_{16}$, $Py_{76.5}Pt_{10}Ag_{13.5}$, $Py_{74}Pt_{15}Ag_{11}$, $Py_{71}Pt_{25}Ag_4$, and $Py_{71}Pt_{29}$, corresponding to the red circles in Fig. 6(a). As seen from the figure, these concentrations will supposedly yield a near-constant M_S of 0.72 T. Using FMR measurements, analyzed in the same way as in Sec. IV A above, we experimentally confirm this prediction by showing a value of $\mu_0 M_S = 0.724 \pm 0.014$ T for all films [inset of Fig. 6(a)]. Moreover, the damping constant within

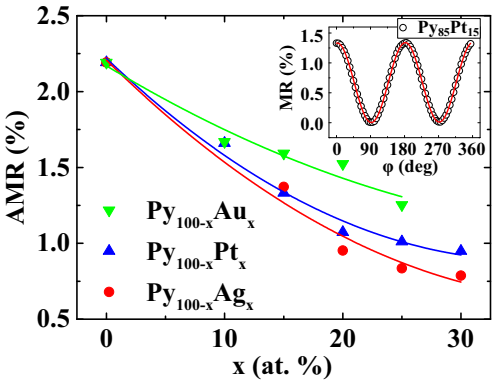

FIG. 5. (Color online) AMR vs composition for $Py_{100-x}Au_x$, $Py_{100-x}Ag_x$, and $Py_{100-x}Pt_x$ films. Solid lines are parabolic fits. Inset: example of an angular measurement together with a fit (red line).

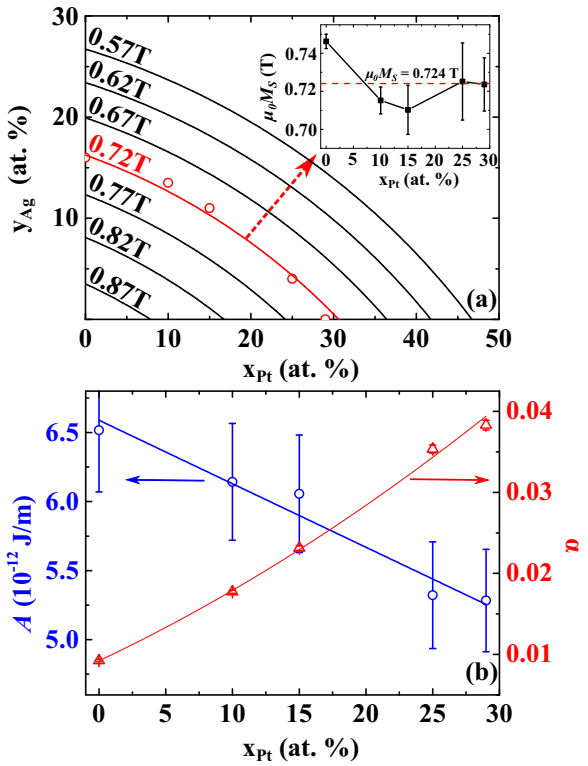

FIG. 6. (Color online) (a) Calculation of the Ag and Pt concentrations for constant values of $\mu_0 M_S$ in multi-alloyed $Py_{100-x-y}Pt_xAg_y$ films. Red circles in (a) represent the compositions of $Py_{100-x-y}Pt_xAg_y$ films chosen for our experiment. The inset of (a) shows the resulting $\mu_0 M_S$ of the sputtered films, as determined from FMR, where the dashed line marks the average value of $\mu_0 M_S$ = 0.724 T. (b) Measurement of the exchange stiffness A and damping α as a function of the Pt concentration for the $Py_{100-x-y}Pt_xAg_y$ films. Solid lines are guides to the eye.

this set of samples increases by a factor of 4 with increasing Pt concentration, in agreement with the results on $Py_{100-x}Pt_x$ films. The exchange stiffness decreases moderately as it can be expected from the decreasing concentration of Py in these films. These results prove that it is possible to accurately choose a desired combination of the parameters M_S and α for the material system $Py_{100-x-y}Pt_xAg_y$. It is also noteworthy that while the original binary alloy films were deposited on glass substrates, the $Py_{100-x-y}Pt_xAg_y$ films were deposited on Si/SiO2 substrates. We can hence conclude that the magnetodynamic properties, and their tailoring, is quite robust in Py based films.

V. CONCLUSIONS

Using both FMR and *ab initio* calculations, we studied the magnetodynamic properties of $Py_{100-x}M_x$ films, with M = Pt, Au, or Ag. From the field dependence of the FMR mode we extracted the saturation magnetization (M_S), damping (α), and inhomogeneous broadening (ΔH_0). From the field dependence of the first PSSW mode, we determined the exchange stiffness (A). M_S and A were found to decrease with increasing alloying, most significantly for Au and least for Pt. While α increases rapidly with increasing Pt content, it is virtually independent of Ag content. *Ab initio* calculations using the coherent potential approximation (CPA) reproduced, and gave a deeper insight into, the experimental trends. Furthermore, the physical origins of the trends in the observed parameters are all qualitatively explained by analyzing the differences in magnetic susceptibility, exchange, chemical bonding, and spin-orbit coupling of Pt, Au, and Ag. Finally, we are able to control both α and M_S of $Py_{100-x-y}Pt_xAg_y$ films independently by alloying with different concentrations of Pt and Ag. We believe that this level of control of critical magnetodynamic material properties in easily sputtered permalloy based alloys will be useful in a wide range of spin torque, spin Hall, and magnonic devices.

ACKNOWLEDGMENTS

We acknowledge financial support from the China Scholarship Council (CSC), the Göran Gustafsson Foundation, the Swedish Research Council (VR), Energimyndigheten (STEM), the Knut and Alice Wallenberg Foundation (KAW), the Carl Tryggers Foundation (CTS), and the Swedish Foundation for Strategic Research (SSF). This work was also supported by the European Research Council (ERC) under the European Communitys Seventh Framework Programme (FP/2007-2013)/ERC Grant 307144 "MUSTANG".

[1] V. V. Kruglyak, S. O. Demokritov, and D. Grundler, J. Phys. D: Appl. Phys. **43**, 260301 (2010).
[2] S. Neusser and D. Grundler, Adv. Mater. **21**, 2927 (2009).
[3] F. Bloch, Z. Phys. **61**, 206 (1930).
[4] J. H. E. Griffiths, Nature (London) **158**, 670 (1946).
[5] J. R. Eshbach and R. W. Damon, Phys. Rev. **118**, 1208 (1960).
[6] R. W. Damon and H. Van De Vaart, J. Appl. Phys. **36**, 3453 (1965).
[7] J. O. Rantschler, R. D. McMichael, A. Castillo, A. J. Shapiro, W. F. Egelhoff, B. B. Maranville, D. Pulugurtha, A. P. Chen, and L. M. Connors, J. Appl. Phys. **101**, 033911 (2007).
[8] G. Woltersdorf, M. Kiessling, G. Meyer, J.-U. Thiele, and C. H. Back, Phys. Rev. Lett. **102**, 257602 (2009).
[9] B. A. Kalinikos and A. N. Slavin, J. Phys. C: Solid State Phys. **19**, 7013 (1986).
[10] J. Slonczewski, J. Magn. Magn. Mater. **159**, L1 (1996).
[11] L. Berger, Phys. Rev. B **54**, 9353 (1996).
[12] D. Ralph and M. Stiles, J. Magn. Magn. Mater. **320**, 1190 (2008).
[13] J. Slonczewski, J. Magn. Magn. Mater. **195**, L261 (1999).
[14] M. Tsoi, A. Jansen, J. Bass, W. Chiang, V. Tsoi, and P. Wyder, Nature (London) **406**, 46 (2000).
[15] M. A. Hoefer, M. J. Ablowitz, B. Ilan, M. R. Pufall, and T. J. Silva, Phys. Rev. Lett. **95**, 267206 (2005).
[16] M. Madami, S. Bonetti, G. Consolo, S. Tacchi, G. Carlotti, G. Gubbiotti, F. B. Mancoff, M. A. Yar, and J. Åkerman, Nat. Nanotechnol. **6**, 635 (2011).

[17] S. Bonetti, V. Tiberkevich, G. Consolo, G. Finocchio, P. Muduli, F. Mancoff, A. Slavin, and J. Åkerman, Phys. Rev. Lett. **105**, 217204 (2010).

[18] S. Bonetti, V. Puliafito, G. Consolo, V. S. Tiberkevich, A. N. Slavin, and J. Åkerman, Phys. Rev. B **85**, 174427 (2012).

[19] R. K. Dumas, E. Iacocca, S. Bonetti, S. R. Sani, S. M. Mohseni, A. Eklund, J. Persson, O. Heinonen, and J. Åkerman, Phys. Rev. Lett. **110**, 257202 (2013).

[20] W. H. Rippard, M. R. Pufall, and T. J. Silva, Appl. Phys. Lett. **82**, 1260 (2003).

[21] A. Slavin and V. Tiberkevich, Phys. Rev. Lett. **95**, 237201 (2005).

[22] G. Consolo, L. Lopez-Diaz, L. Torres, and B. Azzerboni, Phys. Rev. B **75**, 214428 (2007).

[23] G. Consolo, B. Azzerboni, L. Lopez-Diaz, G. Gerhart, E. Bankowski, V. Tiberkevich, and A. N. Slavin, Phys. Rev. B **78**, 014420 (2008).

[24] V. E. Demidov, S. Urazhdin, and S. O. Demokritov, Nat. Mater. **9**, 984 (2010).

[25] M. A. Hoefer, T. J. Silva, and M. W. Keller, Phys. Rev. B **82**, 054432 (2010).

[26] S. M. Mohseni, S. R. Sani, J. Persson, T. N. Anh Nguyen, S. Chung, Y. Pogoryelov, and J. Åkerman, Phys. Status Solidi Rapid Res. Lett. **5**, 432 (2011).

[27] S. M. Mohseni, S. R. Sani, J. Persson, T. N. A. Nguyen, S. Chung, Y. Pogoryelov, P. K. Muduli, E. Iacocca, A. Eklund, R. K. Dumas, S. Bonetti, A. Deac, M. A. Hoefer, and J. Åkerman, Science **339**, 1295 (2013).

[28] S. Mohseni, S. Sani, R. Dumas, J. Persson, T. Anh Nguyen, S. Chung, Y. Pogoryelov, P. Muduli, E. Iacocca, A. Eklund, and J. Åkerman, Physica B **435**, 84 (2014).

[29] S. Chung, S. M. Mohseni, S. R. Sani, E. Iacocca, R. K. Dumas, T. N. Anh Nguyen, Y. Pogoryelov, P. K. Muduli, A. Eklund, M. Hoefer, and J. Åkerman, J. Appl. Phys. **115**, 172612 (2014).

[30] E. Iacocca, R. K. Dumas, L. Bookman, M. Mohseni, S. Chung, M. A. Hoefer, and J. Åkerman, Phys. Rev. Lett. **112**, 047201 (2014).

[31] F. Macià, D. Backes, and A. D. Kent, Nat. Nanotechnol. **9**, 992 (2014).

[32] T. J. Silva and W. H. Rippard, J. Magn. Magn. Mater. **320**, 1260 (2008).

[33] R. K. Dumas, S. R. Sani, S. M. Mohseni, E. Iacocca, Y. Pogoryelov, P. K. Muduli, S. Chung, P. Dürrenfeld, and J. Åkerman, IEEE Trans. Magn. **50**, 4100107 (2014).

[34] R. L. Stamps, S. Breitkreutz, J. Åkerman, A. V. Chumak, Y. Otani, G. E. W. Bauer, J.-U. Thiele, M. Bowen, S. A. Majetich, M. Kläui, I. L. Prejbeanu, B. Dieny, N. M. Dempsey, and B. Hillebrands, J. Phys. D: Appl. Phys. **47**, 333001 (2014).

[35] J. Persson, S. R. Sani, S. Bonetti, F. Magnusson, Y. Pogorylov, S. M. Mohseni, S. Gunnarsson, M. Norling, C. Stoij, and J. Åkerman, IEEE Trans. Magn. **48**, 4378 (2012).

[36] S. R. Sani, P. Dürrenfeld, S. M. Mohseni, S. Chung, and J. Åkerman, IEEE Trans. Magn. **49**, 4331 (2013).

[37] S. Sani, J. Persson, S. M. Mohseni, Y. Pogoryelov, P. K. Muduli, A. Eklund, G. Malm, M. Käll, A. Dmitriev, and J. Åkerman, Nat. Commun. **4**, 2731 (2013).

[38] V. E. Demidov, S. Urazhdin, H. Ulrichs, V. Tiberkevich, A. Slavin, D. Baither, G. Schmitz, and S. O. Demokritov, Nat. Mater. **11**, 1028 (2012).

[39] R. H. Liu, W. L. Lim, and S. Urazhdin, Phys. Rev. Lett. **110**, 147601 (2013).

[40] V. E. Demidov, H. Ulrichs, S. V. Gurevich, S. O. Demokritov, V. S. Tiberkevich, A. N. Slavin, A. Zholud, and S. Urazhdin, Nat. Commun. **5**, 3179 (2014).

[41] Z. Duan, A. Smith, L. Yang, B. Youngblood, J. Lindner, V. E. Demidov, S. O. Demokritov, and I. N. Krivorotov, Nat. Commun. **5**, 5616 (2014).

[42] M. Ranjbar, P. Dürrenfeld, M. Haidar, E. Iacocca, M. Balinskiy, T. Q. Le, M. Fazlali, A. Houshang, A. A. Awad, R. K. Dumas, and J. Åkerman, IEEE Magn. Lett. **5**, 3000504 (2014).

[43] S. Bonetti and J. Åkerman, Top. Appl. Phys. **125**, 177 (2013).

[44] S. Urazhdin, V. E. Demidov, H. Ulrichs, T. Kendziorczyk, T. Kuhn, J. Leuthold, G. Wilde, and S. O. Demokritov, Nat. Nanotechnol. **9**, 509 (2014).

[45] R. K. Dumas and J. Åkerman, Nat. Nanotechnol. **9**, 503 (2014).

[46] S. Lepadatu, J. S. Claydon, C. J. Kinane, T. R. Charlton, S. Langridge, A. Potenza, S. S. Dhesi, P. S. Keatley, R. J. Hicken, B. J. Hickey, and C. H. Marrows, Phys. Rev. B **81**, 020413 (2010).

[47] S. Lepadatu, J. Claydon, D. Ciudad, A. Naylor, C. Kinane, S. Langridge, S. Dhesi, and C. Marrows, Appl. Phys. Express **3**, 083002 (2010).

[48] A. M. Portis, Appl. Phys. Lett. **2**, 69 (1963).

[49] T. E. Hasty, J. Appl. Phys. **35**, 1486 (1964).

[50] A. Conca, J. Greser, T. Sebastian, S. Klingler, B. Obry, B. Leven, and B. Hillebrands, J. Appl. Phys. **113**, 213909 (2013).

[51] H. Ebert, D. Ködderitzsch, and J. Minar, Rep. Prog. Phys. **74**, 096501 (2011).

[52] H. Ebert, The Munich SPR-KKR package, versions 6.3 and 7.2, http://ebert.cup.uni-muenchen.de/SPRKKR.

[53] A. Liechtenstein, M. Katsnelson, V. Antropov, and V. Gubanov, J. Magn. Magn. Mater. **67**, 65 (1987).

[54] H. Ebert and S. Mankovsky, Phys. Rev. B **79**, 045209 (2009).

[55] M. Pajda, J. Kudrnovský, I. Turek, V. Drchal, and P. Bruno, Phys. Rev. B **64**, 174402 (2001).

[56] F. Schreiber and Z. Frait, Phys. Rev. B **54**, 6473 (1996).

[57] A. Brataas, Y. Tserkovnyak, and G. E. W. Bauer, Phys. Rev. Lett. **101**, 037207 (2008).

[58] H. Ebert, S. Mankovsky, D. Ködderitzsch, and P. J. Kelly, Phys. Rev. Lett. **107**, 066603 (2011).

[59] S. Mankovsky, D. Ködderitzsch, G. Woltersdorf, and H. Ebert, Phys. Rev. B **87**, 014430 (2013).

[60] M. E. J. Newman and G. T. Barkema, *Monte Carlo Methods in Statistical Physics* (Clarendon Press, Oxford, 1999).

[61] B. Skubic, J. Hellsvik, L. Nordström, and O. Eriksson, J. Phys. Condens. Matter **20**, 315203 (2008).

[62] S. Mankovsky (private communication).

[63] G. Woltersdorf, Ph.D. thesis, Simon Fraser University, 2004.

[64] N. Mecking, Y. S. Gui, and C.-M. Hu, Phys. Rev. B **76**, 224430 (2007).

[65] C. Herring and C. Kittel, Phys. Rev. **81**, 869 (1951).

[66] J. M. Shaw, H. T. Nembach, T. J. Silva, and C. T. Boone, J. Appl. Phys. **114**, 243906 (2013).

[67] B. Lenk, G. Eilers, J. Hamrle, and M. Münzenberg, Phys. Rev. B **82**, 134443 (2010).

[68] Y. V. Khivintsev, L. Reisman, J. Lovejoy, R. Adam, C. M. Schneider, R. E. Camley, and Z. J. Celinski, J. Appl. Phys. **108**, 023907 (2010).

[69] S. O. Demokritov, B. Hillebrands, and A. N. Slavin, Phys. Rep. **348**, 441 (2001).
[70] I. S. Maksymov and M. Kostylev, Physica E **69**, 253 (2015).
[71] M. van Kampen, C. Jozsa, J. T. Kohlhepp, P. LeClair, L. Lagae, W. J. M. de Jonge, and B. Koopmans, Phys. Rev. Lett. **88**, 227201 (2002).
[72] K. Lenz, H. Wende, W. Kuch, K. Baberschke, K. Nagy, and A. Jánossy, Phys. Rev. B **73**, 144424 (2006).
[73] N. Smith, W. Doyle, D. Markham, and D. LaTourette, IEEE Trans. Magn. **23**, 3248 (1987).
[74] G. Gubbiotti, S. Tacchi, G. Carlotti, P. Vavassori, N. Singh, S. Goolaup, A. O. Adeyeye, A. Stashkevich, and M. Kostylev, Phys. Rev. B **72**, 224413 (2005).
[75] Z. K. Wang, V. L. Zhang, H. S. Lim, S. C. Ng, M. H. Kuok, S. Jain, and A. O. Adeyeye, Appl. Phys. Lett. **94**, 083112 (2009).
[76] S. Ingvarsson, G. Xiao, S. S. P. Parkin, and R. H. Koch, Appl. Phys. Lett. **85**, 4995 (2004).
[77] A. A. Starikov, P. J. Kelly, A. Brataas, Y. Tserkovnyak, and G. E. W. Bauer, Phys. Rev. Lett. **105**, 236601 (2010).
[78] O. Mosendz, J. E. Pearson, F. Y. Fradin, G. E. W. Bauer, S. D. Bader, and A. Hoffmann, Phys. Rev. Lett. **104**, 046601 (2010).
[79] M. Bolte, M. Steiner, C. Pels, M. Barthelmeß, J. Kruse, U. Merkt, G. Meier, M. Holz, and D. Pfannkuche, Phys. Rev. B **72**, 224436 (2005).
[80] T. McGuire and R. Potter, IEEE Trans. Magn. **11**, 1018 (1975).
[81] T. G. S. M. Rijks, S. K. J. Lenczowski, R. Coehoorn, and W. J. M. de Jonge, Phys. Rev. B **56**, 362 (1997).